

Estimating the quasi-Fermi level of holes at the surface of semiconductor photoanodes using outer-sphere redox couples

Received: 7 August 2023

Accepted: 3 April 2025

Published online: 17 April 2025



Yuu Shioiri¹, Keisuke Obata¹, Yudai Kawase¹, Tomohiro Higashi², Masao Katayama^{1,3}, Markus Schleuning⁴, Roel van de Krol⁴, Dennis Friedrich⁴, Fatwa Firdaus Abdi⁵ & Kazuhiro Takanabe¹✉

Semiconductor electrodes can catalyze photo-induced redox reactions with light illumination. Photoexcitation produces excited carriers that subsequently transfer to the front and back contacts as determined by the bulk and surface properties of the photoelectrodes. This transfer defines the resultant quasi-Fermi levels of the photo-generated carriers at the photoelectrode surface, which, in turn, impacts the efficiency of surface photoelectrochemical reactions. However, determining such quasi-Fermi levels is not a simple task. In this study, we introduce a method for estimating the quasi-Fermi level of holes using outer-sphere electron transfer reactions. The quasi-Fermi level of holes is estimated by linking the oxidation photocurrent on photoanodes to the separately measured electrode potential on a stable metal electrode. Using this method, the quasi-Fermi level of holes at the surface is monitored in response to variations in applied potential and light intensity. This approach effectively separates the photocurrents of the CdS model electrode between surface redox reaction and photocorrosion, while concurrently quantifying the dynamic quasi-Fermi level at the surface. This work facilitates quantitative understanding of photoelectrochemical reactions on semiconductor electrodes to design green chemical transformation systems.

Photocatalysis using semiconductors represents a promising approach for converting solar energy into chemical energy. The harnessing of visible light within the solar spectrum is vital for effective solar energy conversion. Thus, visible-light-responsive semiconductors with relatively narrow bandgaps, such as metal chalcogenides and nitrides, have been intensively studied for use in water splitting^{1–3} or organic synthesis^{4–6} applications. Nevertheless, these visible-light-responsive semiconductors face efficiency challenges due to factors like self-photooxidation, also known as photocorrosion, and surface carrier recombination^{7–9}. In photocatalysis, the electrochemical potentials of electrons and holes are

significant parameters as they determine which photoelectrochemical (PEC) reactions occur at the surface of photoelectrodes at which rate. On a photoanode made of an n-type semiconductor, PEC oxidation reactions happen at the surface when illuminated. The rates of these oxidation reactions rely on the electrochemical potential, i.e., the quasi-Fermi level (QFL), of photo-generated holes¹⁰. The QFL of holes at the surface of photoanodes, represented as E_F^h , is defined as follows:

$$E_F^h = E_v + \frac{kT}{e} \ln \left(\frac{p_s}{N_v} \right) \quad (1)$$

¹Department of Chemical System Engineering, School of Engineering, The University of Tokyo, Bunkyo-ku, Tokyo, Japan. ²Institute for Tenure Track Promotion, University of Miyazaki, Miyazaki, Japan. ³Environmental Science Center, The University of Tokyo, Bunkyo-ku, Tokyo, Japan. ⁴Institute for Solar Fuels, Helmholtz-Zentrum Berlin für Materialien und Energie GmbH, Berlin, Germany. ⁵School of Energy and Environment, City University of Hong Kong, Kowloon, Hong Kong SAR, China. ✉e-mail: takanabe@chemsys.t.u-tokyo.ac.jp

where p_s , E_v , N_v , k , T , and e represent the density of holes at the surface of photoanodes, the potential of valence band maximum (VBM), effective density of states in the valence band, Boltzmann's constant, absolute temperature, and elementary charge, respectively. Many researchers have been focusing on measuring the QFL of holes. Pinson, for instance, estimated the QFL of a hole at the surface of the photoanode by measuring the potential of a porous Au layer built on a GaP photoanode¹¹. Subsequently, Boettcher's group developed a dual-working-electrode technique to measure the potential of the electrocatalyst on a TiO₂ photoanode. This enabled them to elucidate the energetics and charge-transfer processes at the semiconductor/electrocatalyst interface^{12,13}. This technique was also utilized in a SrTiO₃ photoanode by Chen et al., and they described the relationship between the rate of water oxidation and the surface potential of the SrTiO₃ photoanode¹⁴. Osterloh's group developed a contactless photovoltage measurement technique using vibrating Kelvin probe surface photovoltage (VKP-SPV) spectroscopy. They were successful in measuring the photovoltage of a BiVO₄ photoanode in electrolyte solutions with fast electron donors¹⁵. All these studies, relying on stable metal oxide semiconductors as model semiconductors, indicate that measuring the surface potential of photoanodes contributes to a better understanding of interfacial energetics and charge-transfer processes.

The semiconductor/electrolyte interface has also been investigated using redox couples^{16–20}. Prévot et al. employed redox couples with varying redox potentials to explore the Fermi-level pinning associated with the surface states on a CuFeO₂ photocathode²⁰. Additionally, using simple reactions with different redox potentials proves effective for analyzing more complex reactions on photoanodes, such as competitive reactions of photocorrosion. This is often observed on visible-light-responsive photoanodes like CdS^{18,19,21,22}. Memming evaluated the energetics of the CdS photoanode/electrolyte interface, emphasizing the faradaic efficiencies (FEs) of oxidation of a variety of redox couples¹⁸. Further, Inoue et al. scrutinized the competitive behavior between photocorrosion and oxidation of redox couples with diverse redox potentials on a CdS photoanode, elucidating the photocorrosion tendency based on the standard potentials of redox couples¹⁹. Although reactions of redox couples can simplify the complexity of reactions on photoanodes, reactants for inner-sphere electron transfer reactions, such as halides and sulfides, are often employed together. It is important to note that charge transfer kinetics are highly dependent on the involved surface, which limits the elucidation of surface kinetics on photoelectrodes.

Here, we propose an experimental protocol to evaluate the QFL of holes at the surface of a photoanode using outer-sphere electron transfer of redox couples in acetonitrile (ACN) solutions. This protocol primarily comprises two steps: i) quantifying the oxidation photocurrent of redox species j_{redox} with various redox potentials on a photoanode and ii) estimating the QFL of holes at the surface by correlating the oxidation photocurrent to the separately measured electrode potential on a stable metal electrode, like a Pt plate electrode. In the first step, PEC measurements are conducted to oxidize the redox species on a photoanode, and the selectivity of redox species oxidation is quantified to obtain the j_{redox} . This is necessary because visible-light-responsive photoanodes, such as CdS photoanodes, suffer from photocorrosion due to self-oxidation by photo-generated holes. The selectivity in the competitive behavior between redox species oxidation and photocorrosion is quantified by reducing the oxidized redox species on a metal wire electrode. In the second step, the current density (j)–potential relationship of redox species oxidation on a Pt plate electrode (under dark conditions) is used to evaluate the QFL of holes at the surface of the photoanode. The QFL of holes is estimated by correlating the j_{redox} on photoanodes to the electrode potential of the Pt plate electrode (both of which should have similar active surface areas), under the assumption that the kinetics of the electrochemical oxidation are identical between

the Pt plate electrode and the photoanodes. To make this assumption reasonable, reversible redox couples with outer-sphere electron transfer were chosen as redox probes. This protocol enables us to estimate the QFL of holes under operando conditions.

The measurement protocol was initially established using a 0.05 wt.% niobium-doped titanium dioxide (Nb:TiO₂) photoanode as a model oxide semiconductor. A CdS single-crystal photoanode serves as a model for the visible-light-responsive photoanode due to its superior carrier transport properties in its bulk, as demonstrated through carrier dynamic analysis. The bulk properties were explored by carrier dynamics analysis using an optical-pump terahertz-probe (OPTP) technique, supplemented by a time-resolved microwave conductivity (TRMC) measurement. Subsequently, the developed protocol was applied to the CdS photoanode, validating that the methodology accurately tracks the QFL of holes on the photoanode in response to the imposed potential and light intensity. By estimating the QFL of holes, the surface reactions on the CdS photoanode are differentiated between redox species oxidation and photocorrosion. The refined protocol will yield information on the QFL of holes at the surface of various photoanodes, specifying the oxidation capability of the photoanodes.

Results

Candidate redox couples

In this protocol, we employ redox couples whose oxidation unfolds through an outer-sphere electron transfer because the QFL of holes is estimated by correlating the oxidation photocurrent density on photoanodes to the separately measured electrode potential of a metal electrode (Supplementary Fig. 1). By utilizing outer-sphere redox couples, consistent electrochemical oxidation kinetics can be assumed on both photoanodes and metal electrodes. Firstly, we investigated the electrochemical properties of redox couples using a glassy carbon (GC) electrode as depicted in Fig. 1. The candidates include molecular redox species (2,2,6,6-tetramethylpiperidine 1-oxyl free radical (TEMPO), 4-hydroxy-2,2,6,6-tetramethylpiperidine 1-oxyl free radical (TEMPOL), thianthrene, iodide, and bromide) and metal complexes (ferrocene, tris(3,4,7,8-tetramethyl-1,10-phenanthroline)iron(II) ([Fe(phen-Me₄)₃]²⁺), tris(1,10-phenanthroline)iron(II) ([Fe(phen)₃]²⁺), and tris(2,2'-bipyridine)ruthenium(II) ([Ru(bpy)₃]²⁺)). The mid-point potentials deduced from cyclic voltammograms (CVs) of these redox couples indicate differing redox potentials among the redox species (Fig. 1a, Supplementary Table 1). Among them, the outer-sphere redox species, such as ferrocene, TEMPO, TEMPOL, and thianthrene, are used for the QFL estimation. Figure 1b presents the CVs of TEMPO at various scan rates. Both anodic and cathodic peak currents are amplified with increasing scan rate. Notably, the anodic peak current increases proportionally to the square root of the scan rate (Fig. 1c). Further, the peak potential separation remained nearly the same irrespective of the scan rates (Fig. 1b). These behaviors in CVs are characteristics of a reversible redox system. The peak potential separation was approximately 69 mV, aligning well with the theoretical value of 60 mV in a reversible one-electron-transfer system at 25 °C^{23,24}. Thianthrene also showed the characteristics of a reversible redox system (Supplementary Fig. 2). To explore the oxidation kinetics of these redox species, we conducted linear sweep voltammetry (LSV) using Pt and GC plate electrodes (Fig. 1d). The oxidation kinetics of ferrocene were virtually identical on both the Pt and GC plate electrodes, indicating that ferrocene oxidation occurs via an outer-sphere electron transfer. In the case of oxidation of TEMPO, TEMPOL, and thianthrene, the LSV curves were not substantially different between the Pt and GC plate electrodes, with a mere difference of approximately 20 mV at 5 mA cm^{−2}, which is far less than the potential difference in the inner-sphere electron transfer, such as oxidation of iodide or bromide (Supplementary Fig. 3). The electrode reaction rate constants of outer-sphere electrode reactions exhibited no significant difference on Pt and GC electrode or on GC electrodes with or without surface modification by monolayer organic molecules^{25,26}. Therefore, we

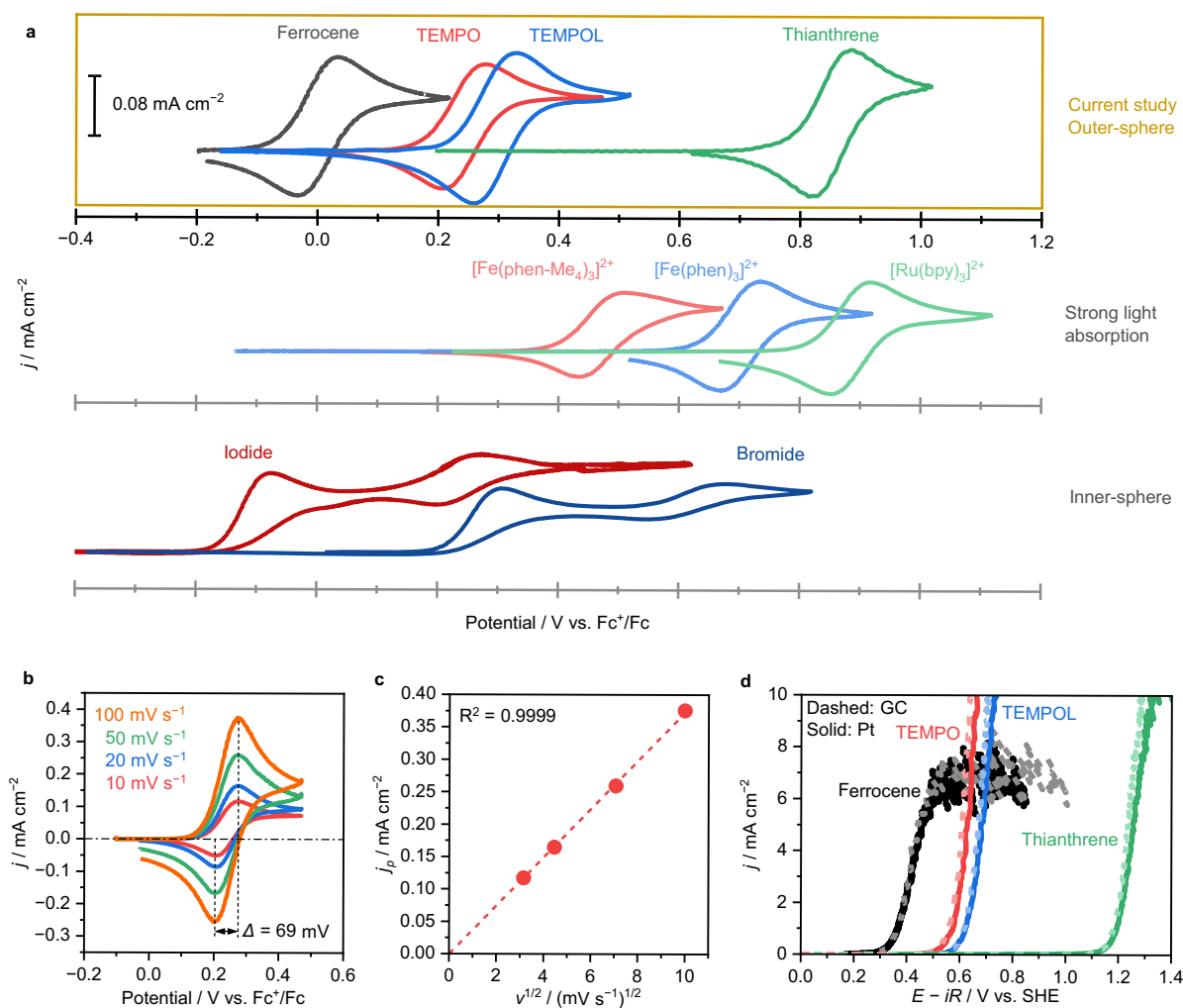


Fig. 1 | Electrochemical properties of redox species. a CVs on the GC disk electrode in 1 mM redox species containing solutions at the scan rate of 10 mV s^{-1} without stirring. **b** CVs on the GC disk electrode in 1 mM TEMPO-containing solution at various scan rates without stirring. **c** The plots of anodic peak current density versus the square root of the scan rate. WE: GC disk; CE: Pt wire; RE: Ag/Ag^+ reference electrode; Electrolyte: ACN containing 100 mM TBAPF₆ and 1 mM of

redox species. **d** Linear sweep voltammetry (LSV) on the Pt plate (solid line) and GC plate (dashed line) electrodes in ACN containing 20 mM ferrocene, 80 mM TEMPO, 80 mM TEMPOL, or 20 mM thianthrene and 100 mM TBAPF₆ with stirring at 700 rpm. CE: Pt wire; RE: Ag/Ag^+ reference electrode. Source data are provided as a Source Data file.

conclude that when using these outer-sphere redox species, it is reasonable to assume that their electrochemical oxidation kinetics are equivalent on both photoanodes and metal electrodes.

Parasitic light absorption by the redox couples is a crucial factor during experimental conditions. In this investigation, we used ferrocene, TEMPO, TEMPOL, and thianthrene as redox couples, because they possess adequately small absorption coefficients for achieving sufficient photocurrent on photoanodes. Other redox couples, like the metal complexes of bipyridine or phenanthroline ligands, exhibit considerably large absorption coefficients, as demonstrated in Supplementary Fig. 4. Our three-electrode cell used in this study has an approximate optical path length of 5 mm (Supplementary Fig. 5). Therefore, it is necessary for the absorption coefficients of the redox couples to be small enough to diminish parasitic absorption and measurement time needed to accumulate a sufficient amount of oxidized redox species. This measure helps evade experimental errors such as ACN evaporation. Improvements in the measurement setup, like introducing back illumination to semiconductor films (which are deposited on a transparent conducting electrode), would

permit the use of redox couples with large absorption coefficients. Nevertheless, in this study, we adopted front light illumination using single-crystal semiconductor photoanodes as model photoanodes.

Estimation of the QFL of holes at the surface of a TiO_2 photoanode

In utilizing the chosen redox couples, an estimation of the QFL of holes was successfully demonstrated, using a 0.05 wt.% niobium-doped titanium dioxide ($\text{Nb}:\text{TiO}_2$) single-crystal photoanode. This protocol entailed quantifying the oxidation of redox couples via reduction on a metal electrode, enabling the derivation of FEs for redox couple oxidation on the photoanode. It is pivotal to maintain a balance between photocurrent densities and diffusion-limiting current densities, as the QFL of holes cannot be distinctly determined if the photocurrent density on a photoanode surpasses the diffusion-limiting current density of redox species. Supplementary Fig. 6 illustrates the LSVs on the GC plate electrode in 10 and 20 mM ferrocene-loaded solutions. The current density obtained from ferrocene oxidation reaches saturation at the potential above roughly 0.5 V versus standard

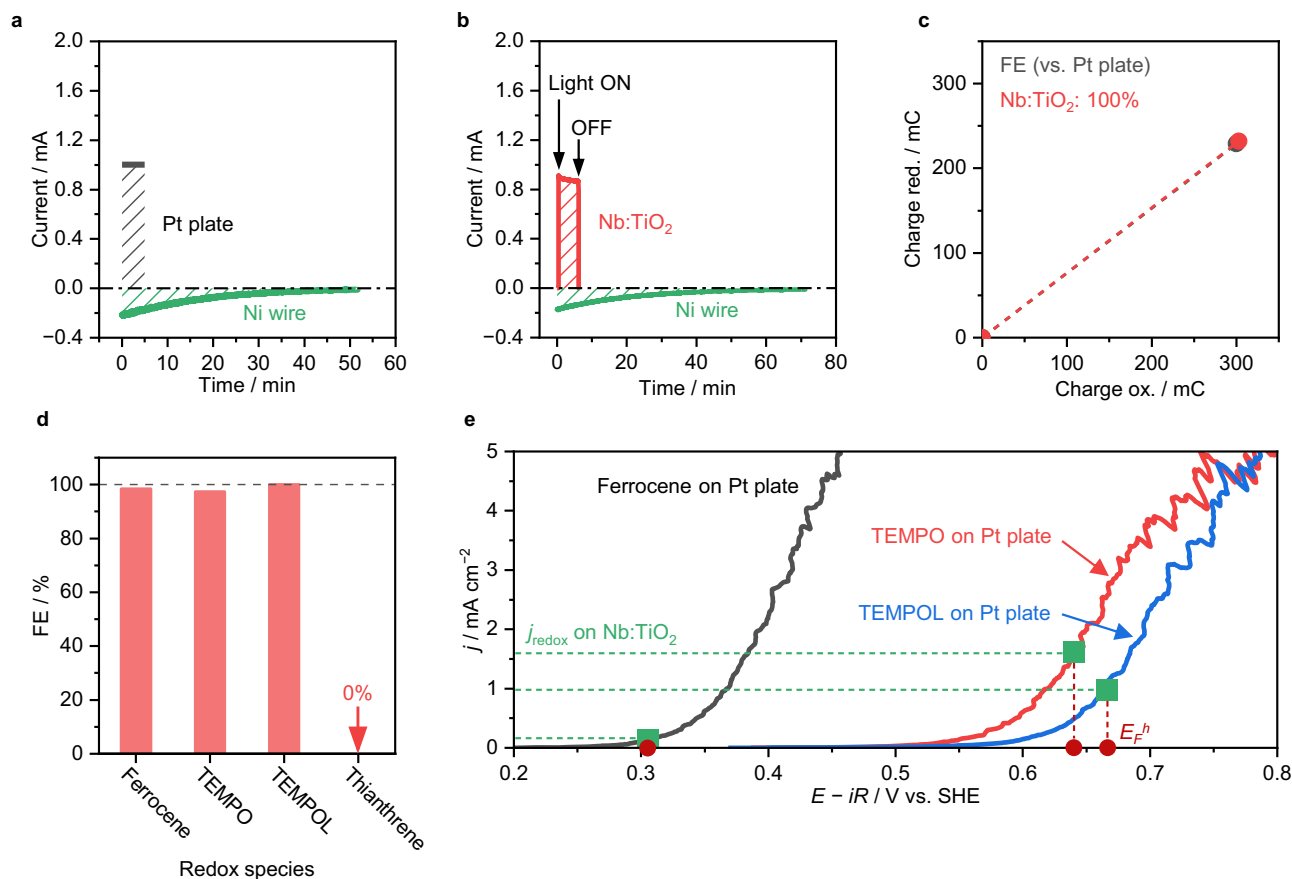


Fig. 2 | Estimation of the QFL of holes on a Nb:TiO₂ photoanode. a i - t curves of chronopotentiometry (CP) for the Pt plate electrode at 1.0 mA to oxidize TEMPOL (black line) and the subsequent CA for the Ni wire electrode at -0.35 V vs. Fc^+/Fc (green line). **b** i - t curves of CA for the Nb:TiO₂ photoanode at -0.08 V vs. Fc^+/Fc to oxidize TEMPOL (red line) and the subsequent CA for the Ni wire electrode at -0.35 V vs. Fc^+/Fc (green line). CE: Pt wire; RE: Ag/Ag⁺ reference electrode;

Electrolyte: ACN containing 20 mM TEMPOL and 100 mM TBAPF₆; stirring rate: 700 rpm; light source: 370 nm LED light (68 mW cm⁻²). **c** Comparison of the results of the Pt plate electrode and the Nb:TiO₂ photoanode. **d** FEs for the oxidation of the redox species on the Nb:TiO₂ photoanode. **e** Estimation of the QFL of holes on the Nb:TiO₂ photoanode during the redox couple oxidation. Source data are provided as a Source Data file.

hydrogen electrode (SHE), indicative of diffusion limitation. The fluctuations in the photocurrent densities are likely due to electrolyte solution stirring. The plateau values shown in Supplementary Fig. 6 represent the upper photocurrent limits for photoanode experiments with these redox couples. If the photocurrent density surpasses the diffusion-limiting current density, the partial current density of redox species oxidation j_{redox} on photoanodes must conform to this diffusion-limiting current density. Consequently, the QFL of holes can be allocated to any potential above 0.5 V vs SHE, without explicit specification. Therefore, careful considerations of the concentrations of redox couples, applied potential on photoanodes, and light intensity are crucial in this protocol to ensure photocurrent densities stay below the diffusion-limiting current densities.

Figure 2a–c present the outcomes of a typical measurement protocol, namely, the oxidation of TEMPOL on the Nb:TiO₂ photoanode. Initially, the Pt plate electrode served as a calibrator to oxidize TEMPOL to TEMPOL⁺ until roughly 300 mC had passed through the circuit. This was followed by the reduction of TEMPOL⁺ on a Ni wire electrode. Control experiments without redox species ensured lack of reduction current associated with the reduction of ACN or any impurity like trace H₂O in the range of applied potential from -0.7 V to 0 V vs. Fc^+/Fc . Thus, in this study we used Pt, Ni, and Au as an electrode for reduction reaction (Supplementary Fig. 7). Subsequently, the oxidation of TEMPOL took place on the Nb:TiO₂ photoanode under 370 nm LED light illumination through a chronoamperometry (CA) measurement set at -0.08 V vs. Fc^+/Fc (0 V vs. Ag/Ag⁺), resulting in a

relatively stable photocurrent (Fig. 2b, red curve). The generated TEMPOL⁺ was then reduced using the Ni wire electrode. As a control measurement for the reduction of oxidized redox species, CAs were conducted on the Ni wire electrode in ACN with only supporting electrolyte (Supplementary Fig. 8), because not only oxidized redox species but also water traces in ACN can be reduced. The current on the Ni wire electrode due to residues such as water was comparatively small (<3 μA) enough to ignore as a contribution to the currents (~ 0.2 mA). In Fig. 2c, the reduction charge was plotted against the oxidation charge for comparison between the Nb:TiO₂ photoanode and the Pt plate electrode. The results for both electrodes are identical, which implies that the FE of TEMPOL oxidation on the Nb:TiO₂ photoanode is unity. The discrepancy between oxidation and reduction charges may be due to the loss of oxidized redox species from the working electrode (WE) compartment to the counter electrode (CE) compartment via the cation exchange membrane. Figure 2d encapsulates the FEs of redox species oxidation on the Nb:TiO₂ photoanode. Outcomes of the oxidation of ferrocene, TEMPO, and thianthrene, required to obtain the FEs, are displayed from Supplementary Fig. 9 to Supplementary Fig. 11, respectively. It was discovered that the FEs are nearly unity in the oxidation of ferrocene, TEMPO, and TEMPOL, suggesting that the Nb:TiO₂ photoanode can selectively oxidize these redox species. On the other hand, thianthrene was not oxidized on the Nb:TiO₂ photoanode, and an immediate decay of photocurrent was observed (Supplementary Fig. 11). It is likely that charge recombination of excited carriers over this doped sample is so facile that the QFL is

pinned at more negative potential than the redox potential of thianthrene. Based on the gathered FEs and average photocurrent densities ($j_{\text{meas.}}$) during the CA measurements, the partial current densities for oxidation of the redox species (j_{redox}) were calculated as shown in Supplementary Table 2.

The QFL of holes (E_F^h) found at the Nb:TiO₂ photoanode surface during the oxidation of each redox species was approximated by drawing a correlation between j_{redox} and the separately gauged electrode potential of the Pt plate electrode. In Fig. 2e, solid lines illustrate the relationship between j_{redox} for the oxidation and potential under dark conditions on the Pt plate electrode. By creating plots on these lines, dependent on the j_{redox} measured on the Nb:TiO₂ photoanode, the electrochemical potential of holes on the photoanode can be estimated. Since the electrochemical oxidation kinetics are assumed to be identical on both the photoanode and Pt plate electrodes, we can now estimate the electrochemical potential of the holes on the illuminated photoanode by effectively comparing the results in Fig. 2e. Consequently, the green dots render the j_{redox} -potential plots under illuminated conditions on the photoanode when oxidizing each redox species, while the red dots on the x-axis display the QFL of holes E_F^h . The approximated E_F^h values stood at 0.30, 0.64, and 0.67 V vs. SHE in the oxidation of ferrocene, TEMPO, and TEMPOL, respectively. It was noted that the E_F^h inclines towards the positive direction during the oxidation of redox species with an increased positive redox potential, an indication of a greater number of holes accumulating at the photoanode surface. However, the QFL of holes could not reach more positive potentials than the redox potential of thianthrene (1.2 V vs. SHE), which is far more negative than the potential of valence band maximum (VBM) of TiO₂ (−3 V vs. SHE^{27,28}). This indicates the significance of discussion on the QFL for those cases where the VBM position cannot be used for oxidation capability. As such, a measurement method for estimating the QFL of holes has been derived.

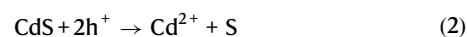
Estimation of the QFL of holes at the surface of a CdS photoanode

In this study, CdS was chosen as a model of visible-light-responsive semiconductor material because of its excellent optoelectronic properties in its bulk form. Initially, the band structure of the CdS was investigated using ultraviolet photoelectron spectroscopy (UPS). The results from the UPS measurement for the CdS single crystal are shown in Supplementary Fig. 12. The work function (ϕ) was calculated to be 3.91 eV, derived from the energy of He I excitation (21.22 eV) and E_{cutoff} in Supplementary Fig. 12a. The potential difference between the Fermi level and VBM was determined from the VB region in the UPS spectra, assuming that the Fermi level (E_{Fermi}) equals the binding energy of 0 eV. Utilizing the reported value of 2.5 eV as the bandgap of CdS²⁹, the band diagram was determined, as shown in Supplementary Fig. 12b. The flat-band potential of the CdS photoanode was determined from the Mott-Schottky plots (Supplementary Fig. 13). The flat-band potential was nearly identical, irrespective of frequency (Supplementary Table 3), averaging at −0.87 V vs. Fc^{+/0} (−0.55 V vs. SHE). This value aligns with the Fermi level of −0.53 V vs. SHE obtained from the UPS measurement. Additionally, Mott-Schottky plots were also obtained in the presence of redox species (Supplementary Fig. 14). If surface states cause the Fermi level to pin, the flat-band potential would shift following the redox potentials of the redox couples in the electrolyte solutions since the surface states would equate to the redox potential²⁰. However, the flat-band potential of the CdS photoanode did not change significantly, regardless of the utilized redox couples (Supplementary Table 4). Therefore, it appears that Fermi-level pinning caused by surface states on the CdS photoanode has a minimal effect on the QFL of holes in the observed potential range.

To understand the fundamental semiconductor properties of a CdS single crystal, an analysis of carrier dynamics was conducted. We

used an OPTP technique and a TRMC measurement (Supplementary Fig. 15). A more detailed discussion of these methods can be found in the Supplementary Information (Supplementary Discussion 1). The measured carrier mobility and diffusion length are summarized in Supplementary Table 6. When compared with the carrier dynamics properties of representative photoanode materials such as Fe₂O₃, BiVO₄, and Ta₃N₅, the CdS single crystal was found to have greater carrier mobility and extended diffusion length, showing that the CdS single crystal exhibits excellent carrier dynamic properties.

Nevertheless, the CdS photoanode is known to suffer from photocorrosion due to its energetically and kinetically facile self-photooxidation reaction. We estimated the QFL of holes on the CdS photoanode to investigate the PEC reactions at the surface of the CdS photoanode. Figure 3a displays the FEs for the oxidation of various redox species oxidation on the Nb:TiO₂, Nb-doped strontium titanate (Nb:SrTiO₃), and CdS photoanodes. Results from this oxidation on the Nb:SrTiO₃ and CdS photoanodes and their subsequent reduction on the metal wire electrodes to determine FEs are displayed in Supplementary Fig. 16–20. As already shown in Fig. 2d, the Nb:TiO₂ photoanode could not oxidize thianthrene, suggesting that its QFL of holes cannot reach sufficiently positive potentials to oxidize thianthrene. Alternatively, a Nb:SrTiO₃ was used as another photoanode for thianthrene oxidation. Here, we chose −0.082 V vs. Fc^{+/0} (0 V vs. Ag/Ag⁺) for the applied potential as a representative value where the photocurrent reached saturation (Supplementary Fig. 21). The FEs of ferrocene oxidation were close to 100% on the CdS photoanodes. This is consistent with the surface morphology of the CdS photoanode as observed by scanning electron microscopy (SEM), showing negligible change before and after the ferrocene oxidation (Supplementary Fig. 22). The photocurrents of ferrocene oxidation were not stable over time on both Nb:TiO₂ and CdS photoanodes, even though the FEs were nearly unity. This may be because a passivating layer of an insoluble iron salt or organic polymer is formed during the oxidation of ferrocene in the ACN solution^{30–32}. However, the estimation of QFL of holes was effectively achieved as discussed in Supplementary Discussion 2. On the contrary, the FEs of TEMPO and TEMPOL oxidation on the CdS photoanode ranged from 85 to 95% respectively, whereas those on the Nb:TiO₂ photoanode were near unity. It is noteworthy that thianthrene, which has a significantly more positive redox potential in comparison to TEMPO and TEMPOL, could be oxidized on the CdS photoanode. The FE of thianthrene oxidation on the CdS photoanode was only 23%, which is considerably lower than the near 100% FE observed on the Nb:SrTiO₃ photoanode. The oxidation of thianthrene was confirmed by UV–vis measurements for reaction solutions (Supplementary Fig. 23). The color of solution clearly changed after the oxidation with the CdS photoanode while the light irradiation at 370 nm alone did not change. Thianthrene radical cation has a characteristic absorption peak at approximately 543 nm^{33,34}. After the oxidation on the CdS photoanode, the absorbance at 543 nm increased, indicating that thianthrene was oxidized to thianthrene radical cation. The increase in the absorbance was smaller than that after the oxidation on the Pt electrode, indicating that thianthrene oxidation competed with photocorrosion on the CdS photoanode. These results suggest that photocorrosion competes with the oxidation of redox species with more positive redox potentials. We confirmed the accuracy of the FE calculated based on the charges of oxidation and reduction by quantifying the dissolved cadmium ions (Cd²⁺) in the electrolyte solution using atomic absorption spectroscopy (AAS) to obtain the FE of photocorrosion competing with TEMPO oxidation. The reaction equation of photocorrosion in the ACN solution can be represented as follows^{35,36}:



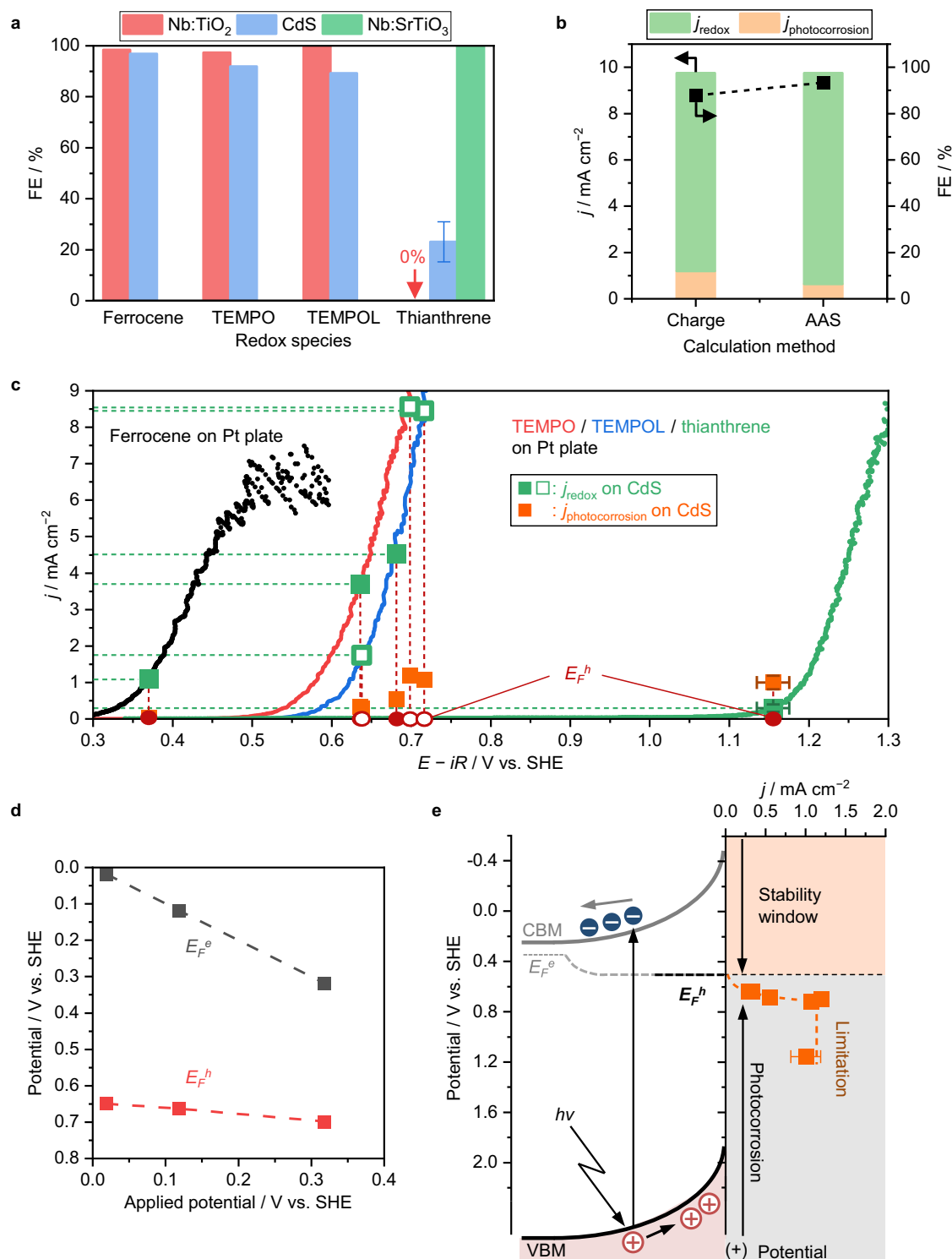


Fig. 3 | Estimation of the QFL of holes on a CdS photoanode. **a** FEs of redox species oxidation on the Nb:TiO₂ (red bar), Nb:SrTiO₃ (green bar), and CdS (blue bar) photoanodes. **b** Comparison of FE and partial current densities calculated from two different methods, charges of oxidation and reduction of TEMPO and quantification of cadmium ions in the reaction solution after the PEC measurements. While the open ones were measured with the light intensity of 17 or 68 mW cm⁻². **c** Estimation of QFL of holes on the CdS photoanode during redox

couple oxidation. **d** Applied potential dependence of the QFL of holes in the TEMPO oxidation. The closed symbols were measured with the light intensity of 34 mW cm⁻² while the open ones were measured with the light intensity of 17 or 68 mW cm⁻². **e** Electronic energy profile of the CdS photoanode combined with the predicted j -potential profile of CdS photocorrosion. Error bars represent standard deviations obtained with three independent experiments. Source data are provided as a Source Data file.

Following this equation, the Cd²⁺ on the surface of the CdS photoanode would dissolve into the reaction solution through photocorrosion. The electrolyte solution after the PEC measurement, shown in Supplementary Fig. 24, was subjected to the AAS

measurement. The quantification results for Cd²⁺ and the calculation of the FE are represented in Supplementary Fig. 25. Figure 3b compares the FEs and partial current densities obtained using charges and AAS. The partial current densities of redox species

oxidation (j_{redox}) and photocorrosion ($j_{\text{photocorrosion}}$) are calculated using the following equations:

$$j_{\text{meas.}} = j_{\text{redox}} + j_{\text{photocorrosion}} \quad (3)$$

$$j_{\text{redox}} = j_{\text{meas.}} \times FE \quad (4)$$

where $j_{\text{meas.}}$ is the average photocurrent density measured in the CA measurements for the CdS photoanode. The FE calculated from charges roughly agrees with that obtained by the AAS result, supporting the validity of the calculation of FEs based on the oxidation and reduction charges.

In Fig. 3c, the QFL of holes at the surface of the CdS photoanode is estimated by correlating the obtained j_{redox} on the CdS photoanode with the electrode potential of a Pt plate electrode. The green-filled square dots depict the j_{redox} on the CdS photoanode for the oxidation of the different redox species by irradiating with a fixed light intensity (34 mW cm^{-2}). The corresponding QFLs of holes are shown as the red-filled circle dots on the x-axis. The QFL of holes shifted to a more positive potential when a redox couple with a more positive redox potential was oxidized. The QFL of holes can be estimated under various conditions, such as the dependence on the light intensity and applied potential. TEMPOL oxidation on the CdS photoanode was performed at different light intensities (17 and 68 mW cm^{-2}) as depicted in Supplementary Fig. 26, and the FEs and partial current densities are summarized in Supplementary Fig. 27. The total photocurrent density almost doubled when the light intensity doubled because the number of excited carriers increased with the increase in light intensity. Conversely, the FE did not significantly change regardless of the light intensity. As a result, both j_{redox} and $j_{\text{photocorrosion}}$ increased in response to the light intensity increase. A similar outcome was also obtained in TEMPO oxidation (Supplementary Fig. 28, 29). The extra j_{redox} on the CdS photoanode and the corresponding E_F^h are plotted as green open square and red open-circle dots, respectively, in Fig. 3c. All j_{redox} and $j_{\text{photocorrosion}}$ plotted in Fig. 3c are summarized in Supplementary Table 7. Supplementary Fig. 30 shows the light intensity dependence of the QFL of holes during TEMPOL oxidation. The QFL of holes linearly shifted in relation to the logarithmic scale of light intensity, consistent with the definition of the QFL of holes when the density of holes at the surface is assumed to change linearly with the light intensity. The dependence of the QFL of holes on the applied potential was also observed during the TEMPOL oxidation. The FEs and partial current densities are represented in Supplementary Fig. 31. The estimated QFLs of holes and electrons are plotted against the applied potential in Fig. 3d. Here, the QFL of electrons can be approximated to the applied potential because the electron is the majority carrier in the CdS photoanode. A higher applied potential leads to a wider space charge region, a larger potential drop across it, and the accumulation of holes at the surface, which in turn leads to a positive shift of the QFL of holes (see Supplementary Discussion 3). The shift of the QFL of holes was, however, much smaller than the shift of the QFL of electrons, and the gained photovoltage decreased with the increase in the applied potential. This is probably because the QFL of holes is pinned at the redox potential of TEMPOL (0.64 V vs. SHE from Supplementary Table 1), due to the facile kinetics of TEMPOL oxidation. This behavior of potential dependence was also observed in the QFL of holes estimated from LSV curve for TEMPOL oxidation on the CdS photoanode (Supplementary Fig. 32). While the applied potential was swept from 0.8 V to -0.4 V vs. SHE , the QFL of holes shifted from 0.69 V to 0.42 V vs. SHE . The behavior of the QFL of holes is similar to the pinning of the front surface potential (E_{Ff}) on the bismuth vanadate (BiVO_4) photoanode, observed using a VKP-SPV technique by Osterloh's group¹⁵. They found that the E_{Ff} is pinned to the electrochemical potential of

the present redox couple in the electrolyte solution under open circuit conditions, due to the rapid hole transfer from the photoanode. This data confirms that the proposed protocol can track the QFL of holes on photoanodes under operando conditions.

In addition, the estimation of the QFL of holes clarifies the relationship between $j_{\text{photocorrosion}}$ and E_F^h (indicated by orange-filled square dots), enabling predictions concerning the kinetics of the CdS photocorrosion. Figure 3e outlines the electronic energy profile of the CdS photoanode in conjunction with the predicted kinetics of CdS photocorrosion. CdS photocorrosion commences as soon as 0.54 V vs. SHE , indicating that competition with photocorrosion is unavoidable when the QFL of holes is more positive than 0.54 V vs. SHE on a bare CdS photoanode. The thermodynamic potential of the CdS photocorrosion in an aqueous solution has been computationally predicted to be 0.25 V vs. SHE ³⁷. The Gibbs free energy for the transfer of Cd^{2+} from water to ACN has been reported to be $17\text{--}42 \text{ kJ mol}^{-1}$ ^{38–40}. Therefore, the thermodynamic potentials of the CdS photocorrosion in an ACN solution are estimated to fall between $0.34\text{--}0.47 \text{ V vs. SHE}$. The predicted onset potential of the CdS photocorrosion aligns with the calculated thermodynamic potential of the photocorrosion. It is noteworthy that the rate of photocorrosion did not increase monotonically as a function of the QFL of holes. The limitation of the $j_{\text{photocorrosion}}$ may indicate that photocorrosion on the CdS photoanode is not controlled by the electrochemical driving force from the holes. The photocorrosion of CdS accumulates solid sulfur as an oxidized product, which limits the kinetics of further oxidation of the CdS surface^{21,41}. Due to the limitation of the $j_{\text{photocorrosion}}$, the QFL of holes reached approximately 1.2 V vs. SHE . This result indicates the benefit of this QFL measurement by outer-sphere reaction because the kinetics of e.g., photocorrosion and Faradaic reaction can be quantitatively discussed.

Discussion

The current study has developed a protocol aimed at estimating the QFL of holes at the surface of photoanodes under operando conditions. This process utilizes reversible redox couples with outer-sphere electron transfer. Experiments were conducted with a Nb:TiO_2 photoanode to confirm the efficacy of the measurement protocol in estimating the QFL of holes during the redox species oxidation process. The QFL estimation on the Nb:TiO_2 photoanode revealed that the QFL of holes cannot reach more positive values than the redox potential of thianthrene, suggesting that the photoanode's capability to drive oxidation reactions is lower than might be expected from the position of its VBM. By implementing this protocol, estimations were made regarding the QFL of holes at the surface of the CdS photoanode which exhibits excellent carrier transport properties evidenced by the analysis of carrier dynamics. These calculations were influenced by light intensity and applied potential. Further, the QFL estimation of holes on the CdS photoanode decoupled the photocurrent kinetics of CdS photocorrosion and the oxidation reaction. The separation of these kinetics unveiled the stability window and oxidation capability of photoanodes with Faradaic efficiency. Utilizing the insights derived from the QFL estimation, it will be possible to select an appropriate reaction or to quantitatively assess and rationally design the performance of protective layers. Furthermore, with regard to (photo)electrocatalytic reactions involving inner-sphere reactions, assuming that an electrocatalyst layer is coated similarly on both semiconductor and conductive substrates, the j - V curve measurements using the catalyst-coated conductive substrate would help to elucidate the QFL on the electrocatalyst-coated semiconductor from its j - V measurements (+Faradaic efficiency measurement) under light irradiation. The estimated QFL will also facilitate understanding of what drives the charge carriers towards the interface. In conclusion, the developed method proves to be useful for designing green chemical transformation systems.

Methods

Preparation of photoanodes and metal electrodes

A commercially available 0.05 wt.% Nb:TiO₂ single crystal ((110), 10 × 10 mm, 0.5 mm thickness, SHINKOSHA Co., Ltd.), 0.01 wt.% Nb:SrTiO₃ single crystal ((100), 10 × 10 mm, 0.5 mm thickness, SHINKOSHA Co., Ltd.), and a CdS single crystal ((0001), 10 × 10 mm, 1 mm thickness, MTI Corp.) were used for photoanodes. The CdS single crystal was cut into pieces to be used as a CdS photoanode. An electrical connection was established between the lead wire and the single crystals by soldering indium onto the edge of the back side of the crystals. This indium soldering was then covered with epoxy resin for insulation. The exposed photoanode surface area, used to calculate the current density, was determined using ImageJ software (Nb:TiO₂ photoanode: 0.89 cm²; Nb:SrTiO₃ photoanode: 0.65 cm²; CdS photoanode: 0.69 cm² in ferrocene oxidation, 0.65 cm² in thianthrene oxidation, and 0.35 cm² in other experiments). We also prepared GC and Pt plate electrodes in the same manner as the photoanodes using a commercially available GC plate (10 × 10 mm, 1 mm thickness, Nilaco Co., LTD) and a Pt plate (10 × 10 mm, 0.1 mm thickness, Nilaco Co., LTD). The surfaces of the Nb:TiO₂ and Nb:SrTiO₃ photoanodes was polished using 0.05 μm polishing alumina and then washed with ultrapure water and ACN before the electrochemical measurements. We cleaned the surface of the CdS photoanode by immersing it in concentrated hydrochloric acid (HCl) solution (35.0–37.0% (mass/mass), FUJIFILM Wako Pure Chemical Corp. (Wako)) for 1 min³⁸. The CdS photoanode was then washed with ultrapure water and ACN (99.5+% (mass/mass), Wako). The GC plate electrode was polished with 0.05 μm polishing alumina, and washed with ultrapure water and ACN, while we cleaned the Pt plate electrode by immersing it in aqua regia for 10 s and then washing it with ultrapure water and ACN before the electrochemical measurements.

Electrochemical and PEC measurements

In the ensuing electrochemical and PEC evaluations, all data were collected using a potentiostat system (VMP3, BioLogic Science Instruments). All measurements were conducted at room temperature (ca. 25 °C). The redox potentials of the species were examined by cyclic voltammetry using a GC disk electrode (diameter: 3.0 mm) inside a single-compartment, three-electrode cell equipped with a Pt wire counter electrode and an Ag/Ag⁺ reference electrode (interior electrolyte solution: ACN containing 0.01 M silver nitrate (AgNO₃) and 0.1 M tetrabutylammonium perchlorate (TBAP)). The electrochemical and PEC oxidation of redox species using the Pt plate electrode and photoanodes, respectively, were carried out in a three-electrode H-type cell. The working electrode compartment and the counter electrode compartment were separated by a cation exchange membrane (Nafion 117, Fuel Cell Store). The three-electrode H-type cell was deployed to reliably quantify the redox species oxidized at the working electrode, as the reduced products at the counter electrode could react with the oxidized redox species. The working electrode was situated at the quartz glass window, maintaining a distance of approximately 5 mm from the electrode and the window. An Ag/Ag⁺ reference electrode was placed in the working electrode compartment, and a coiled-Pt wire was used as the counter electrode. The electrolyte solution in the counter electrode compartment was ACN containing 0.1–0.2 M tetrabutylammonium hexafluorophosphate (TBAPF₆, 98%, Tokyo Chemical Industry Co., Ltd. (TCI)) based on the electrolyte solution in the working electrode compartment. The electrolyte solution in the working electrode compartment is clarified in the captions. The primarily used redox species in this protocol, such as ferrocene (98%, Sigma-Aldrich), 2,2,6,6-tetramethylpiperidine-1-oxyl (TEMPO, 98%, Sigma-Aldrich), 4-hydroxy-2,2,6,6-tetramethylpiperidine 1-oxyl free radical (TEMPOL, 98%, TCI), and thianthrene (>98%, TCI) were readily available commercially and used without any modification. In all electrochemical and PEC measurements using the H-type cell, the volume

of the electrolyte solution was 40 mL in both the working and counter electrode compartments. All electrochemical and PEC measurements were performed under an Ar atmosphere.

Before we initiated the oxidation of the redox species on the photoanodes and the Pt plate electrode, we conducted electrochemical measurements to establish the standard condition of the electrolyte solutions. The fresh electrolyte solution contained only reduced redox species. Conversely, the electrolyte solution in its standard condition contained a certain portion of the oxidized redox species.

To create this standard condition, we first conducted CA using a Pt wire electrode at 2–3 mA. This action oxidized the redox species until ~300 mC of charge had passed through the circuit. Subsequently, we switched the working electrode to a metal wire reduction electrode and conducted CA at the applied potential within the potential window (Supplementary Fig. 7). This was done until the reduction current on the metal wire electrode decreased to a threshold current (*I*_{th}), which was set to −0.01 mA in our setup.

The oxidation of redox species on the Pt plate electrode and photoanode commenced from this standard condition. The reduction of the oxidized redox species continued until the electrolyte solution returned to the standard condition. This procedure was chosen because reducing the oxidized redox species to the same condition as the fresh electrolyte solution would take a significantly longer time.

After preparing the standard condition of electrolyte solutions, we conducted electrochemical measurements with the Pt plate electrode and PEC measurements with photoanodes to determine FEs of redox species oxidation. We employed an LED light (370 nm, ASAHI SPECTRA Co., Ltd.) as the light source for the PEC measurements, positioning it 1 cm away from the photoanodes. The optical path length in the electrolyte solution was ~5 mm. CP and CA were performed on the Pt plate electrode and photoanodes, respectively, to oxidize redox species until the circuit had a charge pass-through of around 300 mC. Subsequently, we replaced the working electrode with the metal wire electrode and reduced the oxidized redox species back to the electrolyte solution's standard condition. The faradaic efficiency of redox species oxidation was determined by the following equation:

$$FE/\% = \frac{C_{\text{red, after photoanodes}}/C_{\text{ox, photoanodes}}}{C_{\text{red, after Pt plate}}/C_{\text{ox, Pt plate}}} \times 100 \quad (5)$$

The charge of the redox species oxidation (*C*_{ox}) was obtained by integrating the current on photoanodes and Pt plate electrodes over time. The charge of the reduction of the oxidized redox species (*C*_{red}) was obtained by integrating the current on the metal wire electrode over time. The applied currents and potentials in CP and CA measurements, respectively, were described in the captions.

The conversion of the electrode potential from Ag/Ag⁺ to ferrocene/ferrocene (Fc⁺/Fc) is based on the CVs for 1 mM ferrocene with the GC disk electrode⁴², and *E*(Fc⁺/Fc) is 0.08 V vs. Ag/Ag⁺. The electrode potential of Fc⁺/Fc is converted to the SHE by *E*(Fc⁺/Fc) = 0.40 V vs. SHE⁴³. The LSV curves on the Pt plate electrode, which were used to estimate the QFL of holes on photoanodes, were *iR*-corrected using uncompensated resistances between the working and the reference electrodes. The uncompensated resistances were obtained from the high frequency intersect (≥100 kHz) in electrochemical impedance spectroscopy measurements (amplitude 10 mV).

OPTP and TRTS

The measurements were taken according to previous literatures^{44–46}. Supplementary Fig. 33 shows a schematic illustration of the reflection mode setup. The CdS single crystal is photoexcited by an ultrafast laser pulse with a full-width half-maximum of ~70 fs at a 150 kHz repetition rate and a wavelength of 400 nm. The setup consists of an amplifier

(150 kHz, RegA, Coherent Corp.), which is seeded by 800 nm pulses from a Ti:Sapphire oscillator (80 MHz, Vitora, Coherent Corp.). An optical rectification in a (110)-oriented ZnTe crystal generates the THz pulse. Detection is conducted in a second ZnTe crystal. Further details are provided in previous literature^{44–46}.

ST-TRMC

The measurements were performed as previous literatures^{44,45}. The differences from conventional TRMC are excitation source, the measurement electronics, the frequency band, and the waveguide design. The excitation source remains the same as that used in the OPTP setup. An oscilloscope (RTO2044, Rohde and Schwarz) is used to detect changes in reflected microwave power, with a sampling rate of 20 Gs s⁻¹ and a bandwidth of 4 GHz. The microwave can vary in frequency between 28 and 38 GHz and is chosen to ensure that the reflected power is at a minimum. In this particular setup, the sample is positioned on top of the waveguide, which does not have an iris, effectively allowing the sample to terminate the waveguide. This setup offers a high time resolution, demonstrated by its short rise time of only 100 ps. However, this advantage comes with the drawback of a relatively poor signal-to-noise ratio. For the ST-TRMC design, it was difficult to determine the precise K-factor, which prevented us from calculating absolute mobilities. Additional details can be found in previous literature^{44,45}.

Other characterization

The band structure of a CdS single crystal was determined by UPS (KRATOS ULTRA2, Shimadzu). Helium I excitation (21.22 eV) was utilized, and a charge neutralizer was employed during the UPS measurement.

The absorption spectra of reaction solutions were obtained by UV-vis measurements (V-770, JASCO Corp.). The surface morphology of the CdS photoanode was characterized before and after oxidation using SEM (JSM-IT800, JEOL Ltd.). A polarized Zeeman atomic absorption spectrophotometer (ZA3000, Hitachi High-Tech Corp.) was utilized for AAS to quantify the cadmium ions in the electrolyte solutions.

Data availability

All data that support the findings of this study can be found within this article and its supplementary information. The source data, backing the findings of this study, are provided with this paper. Any correspondence and material requests should be addressed to K. Takanabe. Source data are provided with this paper.

References

- Higashi, T. et al. Design of semitransparent tantalum nitride photoanode for efficient and durable solar water splitting. *Energy Environ. Sci.* **15**, 4761–4775 (2022).
- Fu, Y. et al. Phase-modulated band alignment in CdS Nanorod/SnS_x nanosheet hierarchical heterojunctions toward efficient water splitting. *Adv. Funct. Mater.* **28**, 1706785 (2018).
- Shiuan Ng, L. et al. Surface-degenerate semiconductor photocatalysis for efficient water splitting without sacrificial agents via a reticular chemistry approach. *Angew. Chem. Int. Ed.* **135**, e202313695 (2023).
- Muralirajan, K. et al. Exploring the structure and performance of Cd-chalcogenide photocatalysts in selective trifluoromethylation. *ACS Catal.* **11**, 14772–14780 (2021).
- Jiang, Y., Wang, C., Rogers, C. R., Kodaimati, M. S. & Weiss, E. A. Regio- and diastereoselective intermolecular [2+2] cycloadditions photocatalysed by quantum dots. *Nat. Chem.* **11**, 1034–1040 (2019).
- Gan, Q. et al. Direct N–H activation to generate nitrogen radical for arylamine synthesis via quantum dots photocatalysis. *Angew. Chem. Int. Ed.* **62**, e202218391 (2023).
- Meissner, D., Memming, R. & Kastening, B. Fundamental problems of water splitting at cadmium sulfide. *Chem. Phys. Lett.* **127**, 419–423 (1986).
- Kawase, Y., Higashi, T., Katayama, M., Domen, K. & Takanabe, K. Maximizing oxygen evolution performance on a transparent NiFeO_x/Ta₃N₅ photoelectrode fabricated on an Insulator. *ACS Appl. Mater. Interfaces* **13**, 16317–16325 (2021).
- Li, K. et al. Evolution of surface oxidation on Ta₃N₅ as probed by a photoelectrochemical method. *ACS Appl. Mater. Interfaces* **13**, 17420–17428 (2021).
- Gerischer, H. The impact of semiconductors on the concepts of electrochemistry. *Electrochim. Acta* **35**, 1677–1699 (1990).
- Pinson, W. E. Quasi-Fermi level measurement in an illuminated GaP photoelectrolysis cell. *Nature* **269**, 316–318 (1977).
- Lin, F. & Boettcher, S. W. Adaptive semiconductor/electrocatalyst junctions in water-splitting photoanodes. *Nat. Mater.* **13**, 81–86 (2014).
- Qiu, J. et al. Direct in situ measurement of charge transfer processes during photoelectrochemical water oxidation on catalyzed hematite. *ACS Cent. Sci.* **3**, 1015–1025 (2017).
- Chen, R. et al. Linking the photoinduced surface potential difference to interfacial charge transfer in photoelectrocatalytic water oxidation. *J. Am. Chem. Soc.* **145**, 4667–4674 (2023).
- Daemi, S., Kundmann, A., Becker, K., Cendula, P. & Osterloh, F. E. Contactless measurement of the photovoltage in BiVO₄ photoelectrodes. *Energy Environ. Sci.* **16**, 4530–4538 (2023).
- Desilvestro, J. & Grätzel, M. Photoelectrochemistry of polycrystalline n-WO₃ electrochemical characterization and photoassisted oxidation processes. *J. Electroanal. Chem. Interf. Electrochem.* **238**, 129–150 (1987).
- Kobayashi, T., Yoneyama, H. & Tamura, H. Influence of the reactivity of reducing agents on anodic photocurrents at TiO₂ electrodes. *J. Electroanal. Chem. Interf. Electrochem.* **124**, 179–188 (1981).
- Memming, R. The role of energy levels in semiconductor-electrolyte solar cells. *J. Electrochem. Soc.* **125**, 117–123 (1978).
- Inoue, T., Watanabe, T., Fujishima, A., Honda, K. & Kohayakawa, K. Suppression of surface dissolution of CdS photoanode by reducing agents. *J. Electrochem. Soc.* **124**, 719–722 (1977).
- Prévo, M. S. et al. Evaluating charge carrier transport and surface states in CuFeO₂ photocathodes. *Chem. Mater.* **29**, 4952–4962 (2017).
- Nakatani, K., Matsudaira, S. & Tsubomura, H. Photoanodic behavior of n-type cadmium sulfide in acetonitrile solutions containing iodide ion. *J. Electrochem. Soc.* **125**, 406–409 (1978).
- Inoue, T., Watanabe, T., Fujishima, A. & Honda, K. Investigation of CdS photoanode reaction in the electrolyte solution containing sulfide ion. *Bull. Chem. Soc. Jpn.* **52**, 1243–1250 (1979).
- Yamada, H., Yoshii, K., Asahi, M., Chiku, M. & Kitazumi, Y. Cyclic voltammetry part 1: fundamentals. *Electrochemistry* **90**, 102005–102005 (2022).
- Sandford, C. et al. A synthetic chemist's guide to electroanalytical tools for studying reaction mechanisms. *Chem. Sci.* **10**, 6404–6422 (2019).
- Tanimoto, S. & Ichimura, A. Discrimination of inner- and outer-sphere electrode reactions by cyclic voltammetry experiments. *J. Chem. Educ.* **90**, 778–781 (2013).
- McCreery, R. L. Advanced carbon electrode materials for molecular electrochemistry. *Chem. Rev.* **108**, 2646–2687 (2008).
- Mulmi, D. D. et al. Optical and electric properties of Nb-doped anatase TiO₂ single crystal. *J. Phys. Chem. Solids* **65**, 1181–1185 (2004).
- Serpone, N. Is the band gap of pristine TiO₂ narrowed by anion- and cation-doping of titanium dioxide in second-generation photocatalysts? *J. Phys. Chem. B* **110**, 24287–24293 (2006).
- Madelung, O. *Semiconductors: Data Handbook* (Springer Berlin, 2012).

30. Kamau, G. N., Saccucci, T. M., Gounili, Giv, Nassar, A.-E. F. & Rusling, J. F. Films formed by oxidation of ferrocene at platinum electrodes. *Anal. Chem.* **66**, 994–1001 (1994).
31. Daschbach, J., Blackwood, D., Pons, J. W. & Pons, S. Electrochemistry of ferrocene in acetonitrile—evidence for irreversible kinetic behavior due to passive film formation. *J. Electroanal. Chem. Interf. Electrochem.* **237**, 269–273 (1987).
32. Zotti, G., Schiavon, G., Zecchin, S. & Favretto, D. Dioxygen-decomposition of ferrocenium molecules in acetonitrile: the nature of the electrode-fouling films during ferrocene electrochemistry. *J. Electroanal. Chem.* **456**, 217–221 (1998).
33. De Sorgo, M., Wasserman, B. & Szwarc, M. Aggregation of salts of thianthrene radical cations. *J. Phys. Chem.* **76**, 3468–3471 (1972).
34. Rapta, P., Kress, L., Hapiot, P. & Dunsch, L. Dimerization of thianthrene radical cations as studied by in situ ESR and UV-Vis-NIR voltammetry at different temperatures. *Phys. Chem. Chem. Phys.* **4**, 4181–4185 (2002).
35. Richard, W. Becquerel photovoltaic effect in binary compounds. *J. Chem. Phys.* **32**, 1505–1514 (1960).
36. Meissner, D., Memming, R. & Kastening, B. Photoelectrochemistry of cadmium sulfide. 1. Reanalysis of photocorrosion and flat-band potential. *J. Phys. Chem.* **92**, 3476–3483 (1988).
37. Bard, A. J. & Wrighton, M. S. Thermodynamic potential for the anodic dissolution of n-type semiconductors: a crucial factor controlling durability and efficiency in photoelectrochemical cells and an important criterion in the selection of new electrode/electrolyte systems. *J. Electrochem. Soc.* **124**, 1706–1710 (1977).
38. Kageshima, Y., Kumagai, H., Minegishi, T., Kubota, J. & Domen, K. A photoelectrochemical solar cell consisting of a cadmium sulfide photoanode and a ruthenium–2,2′-bipyridine redox shuttle in a non-aqueous electrolyte. *Angew. Chem. Int. Ed.* **54**, 7877–7881 (2015).
39. Hedwig, G. R., Owens, D. A. & Parker, A. J. Solvation of ions. XXIV. Entropies of transfer of some divalent metal ions from water to nonaqueous solvents. *J. Am. Chem. Soc.* **97**, 3888–3894 (1975).
40. Marcus, Y. Thermodynamic functions of transfer of single ions from water to nonaqueous and mixed solvents: part I - Gibbs free energies of transfer to nonaqueous solvents. *Pure Appl. Chem.* **55**, 977–1021 (1983).
41. Meissner, D., Benndorf, C. & Memming, R. Photocorrosion of cadmium sulfide: Analysis by photoelectron spectroscopy. *Appl. Surf. Sci.* **27**, 423–436 (1987).
42. Gritzner, G. & Kůta, J. Recommendations on reporting electrode potentials in nonaqueous solvents: IUPAC commission on electrochemistry. *Electrochim. Acta* **29**, 869–873 (1984).
43. Housecroft, C. E. & Sharpe, A. G. Organometallic compounds of d-block elements. in *Inorganic Chemistry* 924–930 (Pearson, 2012).
44. Schleuning, M. et al. Generalized method to extract carrier diffusion length from photoconductivity transients: cases of BiVO₄, halide perovskites, and amorphous and crystalline silicon. *PRX Energy* **1**, 023008 (2022).
45. Schleuning, M. et al. Carrier localization on the nanometer-scale limits transport in metal oxide photoabsorbers. *Adv. Funct. Mater.* **33**, 2300065 (2023).
46. Hempel, H. et al. Predicting solar cell performance from terahertz and microwave spectroscopy. *Adv. Energy Mater.* **12**, 2102776 (2022).

Acknowledgements

This work was financially supported by the Mohammed bin Salman Center for Future Science and Technology for Saudi-Japan Vision 2030 at The University of Tokyo (MbSC2030) (K.T.).

Author contributions

Y.S., K.O., and K.T. conceived the project idea and designed the research. Y.S., K.O., Y.K., T.H., M.K., and K.T. planned the experiments for the estimation of the QFL of holes, and Y.S. executed these experiments. Y.K., M.S., R.v.d.K., D.F., and F.F.A. coordinated the experiments for carrier dynamic analysis, and Y.K. and M.S. carried out these experiments. Y.S. composed the manuscript's initial draft. All authors participated in discussing the results and subsequently reviewed and edited the manuscript.

Competing interests

The authors declare no competing interests.

Additional information

Supplementary information The online version contains supplementary material available at <https://doi.org/10.1038/s41467-025-58837-9>.

Correspondence and requests for materials should be addressed to Kazuhiro Takanabe.

Peer review information *Nature Communications* thanks Min Liu, Nestor Guijarro and the other, anonymous, reviewers for their contribution to the peer review of this work. A peer review file is available.

Reprints and permissions information is available at <http://www.nature.com/reprints>

Publisher's note Springer Nature remains neutral with regard to jurisdictional claims in published maps and institutional affiliations.

Open Access This article is licensed under a Creative Commons Attribution-NonCommercial-NoDerivatives 4.0 International License, which permits any non-commercial use, sharing, distribution and reproduction in any medium or format, as long as you give appropriate credit to the original author(s) and the source, provide a link to the Creative Commons licence, and indicate if you modified the licensed material. You do not have permission under this licence to share adapted material derived from this article or parts of it. The images or other third party material in this article are included in the article's Creative Commons licence, unless indicated otherwise in a credit line to the material. If material is not included in the article's Creative Commons licence and your intended use is not permitted by statutory regulation or exceeds the permitted use, you will need to obtain permission directly from the copyright holder. To view a copy of this licence, visit <http://creativecommons.org/licenses/by-nc-nd/4.0/>.

© The Author(s) 2025